第 49 卷 第 3 期/2022 年 2 月/中国激光 研究论文

中国激光

基于 PIN 二极管的可开关宽带极化转换超表面

李达民[1]，王佳云[1]，苏晓强[2]，董丽娟[2*]，陈新伟[1]，张文梅[1]，杨荣草[1**]

[1]山西大学物理电子工程学院，山西 太原 030006；

[2]山西大同大学微结构电磁功能材料省市共建山西省重点实验室，山西 大同 037009

摘要 为了在宽频内实现可开关的高效率线极化转换，设计了一个嵌入 PIN 二极管的十字架型极化转换超表面。仿真结果显示，当 PIN 二极管处于导通状态时，在 4.03～7.71 GHz 范围内，该超表面的极化转换率超过 90%，相对带宽为 62.7%；当 PIN 二极管处于截止状态时，该超表面在工作频段相当于反射板。通过理论分析和表面电流分布解释了极化转换机理。最后，对所制作样品的实验测量进一步证实了该超表面可开关的极化转换效果。所设计的超表面有望应用于电磁兼容和极化探测等领域。

关键词 材料；超表面；可开关极化转换；PIN 二极管；宽带

中图分类号 O441 **文献标志码** A **doi**：10.3788/CJL202249.0303001

1 引 言

人工电磁超表面的出现[1]，打破了传统电磁材料体积大和成本高的限制，使得自由地控制电磁波成为可能。超表面在科学工程前沿领域已得到广泛应用，包括负折射[2]、隐身斗篷[3]、全息图[4-5]和超构透镜[6]等。而极化作为电磁波最基础和重要的特性之一，在完美吸收[7-8]、非对称传输[9-10]和极化转换[11-13]等领域都有重要的应用。因此，对电磁波的极化状态的控制非常重要。

目前，从微波到可见光波段，很多基于超表面设计的极化转换器被报道，其极化转换功能涵盖线极化到线极化[14-17]、线极化到圆极化[18-21]、圆极化到圆极化[22-23]的转换。例如：Grady 等[11]基于金属栅结构，实现了太赫兹频段的宽频线极化转换性能；Lu 等[15]基于四个 L 型结构，设计出一种工作在太赫兹频段的宽频线极化转换器；Ghosh 等[20]提出一种基于石墨烯的极化转换超表面，可以实现在中红外波段三频段线极化到圆极化的转换；Wang 等[23]基于 Z 型结构单元，设计出一种工作在微波范围的超表面，可以实现圆极化到圆极化转换。另外，工作在远红外和可见光波段的宽频极化转换器也有相关报道[24-25]。上述大多数研究提出的极化转换器虽然实现了多频或宽频的功能，但是一旦结构被制作完成，其功能也随之固定，不具有可调性，这导致这些极化转换器的应用场景较为单一。因此对于可调或可开关的高效宽带极化转化器的研究十分必要。

本文设计出一个嵌入 PIN 二极管的十字型超表面，通过控制单元结构中 PIN 二极管的状态，可以实现可开关的极化转换效果。当 PIN 二极管处于导通状态时，该超表面实现了转换率超过 90%的宽带极化转换，相对带宽为 62.7%；当 PIN 二极管处于截止状态时，该超表面在工作频段相当于反射板。通过理论分析和表面电流分布解释了所设计超表面的极化转换机理，并实验证实了所设计超表面可开关的宽频极化转换功能。

2 结构设计

所设计的可开关宽频线极化转换超表面的结构如图 1 所示。图 1(a)为 6×6 的阵列示意图，其单

收稿日期：2021-05-06；**修回日期**：2021-06-02；**录用日期**：2021-06-18

基金项目：山西省科技创新团队项目(201805D131006)、山西省重点研发计划项目(201903D121026)、山西省研究生教育创新项目(2020SY001)

通信作者：*donglijuan_2012@163.com；**sxdxyrc@sxu.edu.cn

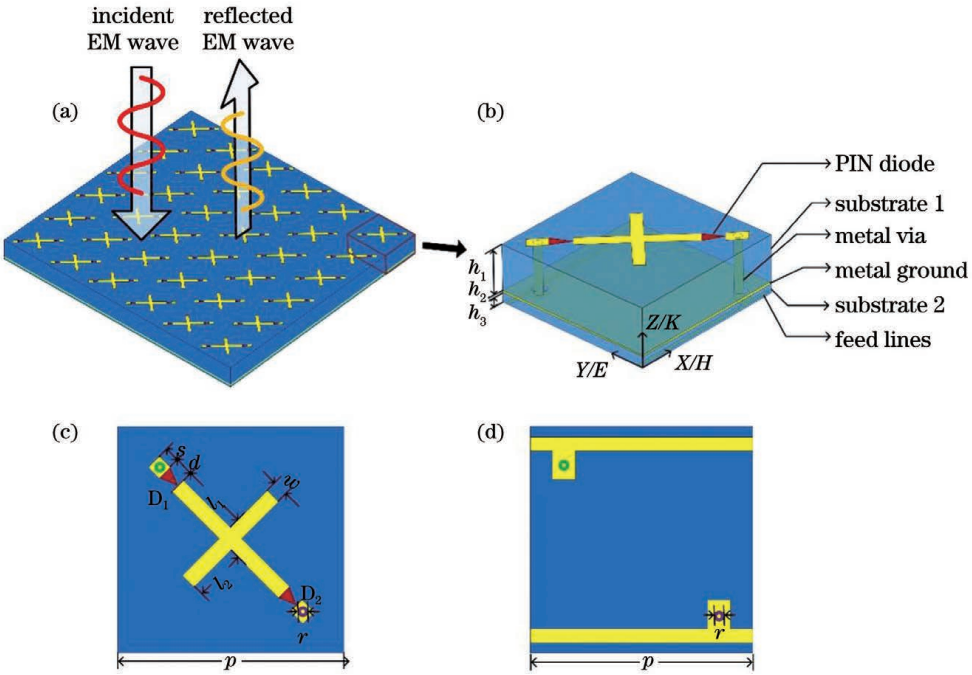

图 1　所设计超表面的结构示意图。(a)6×6 阵列示意图;(b)单元结构示意图;(c)顶层金属谐振单元;(d)底层馈电层

Fig. 1　Schematic of the designed metasurface. (a) Schematic of 6×6 array; (b) schematic of unit cell; (c) resonance cell of top metal; (d) bottom feeder layer

元结构如图 1(b)所示,该结构从上到下依次为顶层的十字架型金属谐振单元、介质层 1、连续的金属薄膜、介质层 2 和底层的馈电层。十字架型金属谐振单元刻蚀在介质层 1 的正面,十字架的长臂沿着单元晶胞的对角线,在长臂中嵌入两个 PIN 二极管(图 1 的三角部分),连续的金属薄膜覆盖在介质层 1 的背面,用来阻挡电磁波的透射,如图1(b)、(c)所示。介质层2是为了解决二极管的馈电问题而引入的,二极管 D_1 的正极和二极管 D_2 的负极分别通过金属过孔和底层的馈电线连接,图 1(d)为底层的馈电层示意图。为了防止金属过孔和铜薄膜接触造成短路,对铜薄膜金属过孔的位置作隔离处理。结构中所有金属均为铜,其电导率为 5.8×10^7 S/m,介质层材质为 FR-4,介电常数为 4.3,正切损耗为 0.025,其他优化后的参数如表 1 所示。

表 1　可开关宽带极化转换超表面的结构参数

Table 1　Structure parameters of switchable broadband polarization conversion metasurface

Parameter	h_1	h_2	h_3	l_1	l_2	w	d	r	p	s
Value /mm	6	0.038	1	4.6	3.6	0.8	2	0.6	15	1

顶层金属谐振单元嵌入的 PIN 二极管为 NXP 公司生产的 BA591[26],根据 BA591 的参数,其导通和截止状态可以分别等效为不同的 RLC 串联电路,如图 2 所示,导通状态可以等效为一个电阻 R_{on} 和电感 L_{on} 的串联电路,截止状态可以等效为电阻 R_{off} 和电容 C_{off} 的串联电路,其中 $R_{on}=0.36\ \Omega$,$L_{on}=2$ nH,$R_{off}=100$ kΩ,$C_{off}=0.65$ pF。

在仿真中,采用 CST 电磁仿真软件对所提出的极化转换超表面进行数值仿真,将 x 轴和 y 轴方向设置为周期性边界条件(unit cell),电磁波沿着 $-z$ 轴方向传播,电场和磁场分别沿着 y 轴和 x 轴方向

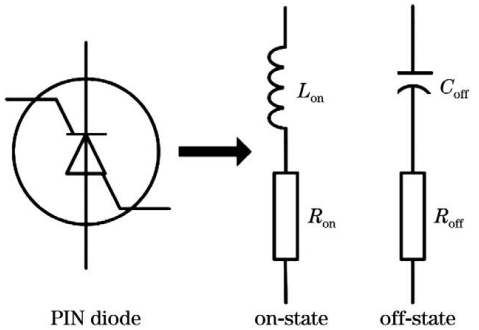

图 2　BA591 二极管在不同状态下的等效电路模型

Fig. 2　Equivalent circuit models of BA591 at different states

传播，如图 1(b)所示。共面极化反射系数和交叉极化反射系数分别定义为 $r_{yy}=|E_{yr}|/|E_{yi}|$ 和 $r_{xy}=|E_{xr}|/|E_{yi}|$，其中 $E_{xi}(E_{xr})$ 和 $E_{yi}(E_{yr})$ 分别为入射(反射)电磁波沿着 x 轴和 y 轴方向的电场分量。因此，极化转换率(polarization conversion rate，PCR；R_{PCR})的求解公式为：$R_{PCR}=|r_{xy}|^2/(|r_{xy}|^2+|r_{yy}|^2)$。

3　结果及分析

由于单元结构中两个二极管 D_1 和 D_2 的方向相同，因此当给二极管施加合适的偏置电压时，D_1 和 D_2 将同时处于导通或截止状态。图 3 所示为当二极管处于不同状态，电场沿着 y 轴方向极化的电磁波垂直入射到所设计超表面时的反射系数以及对应的 PCR。从图 3(a)、(b)可以看到，当二极管处于导通状态时，在 4.03～7.71 GHz 频率范围内，共面极化反射系数 r_{yy} 低于 0.2，交叉极化反射系数 r_{xy} 高于 0.9，对应的 PCR 高于 0.9，此时实现了宽带极化转换，相对带宽达到 62.7%。当二极管处于截止状态时，共面极化反射系数 r_{yy} 高于 0.8，交叉极化反射系数 r_{xy} 低于 0.3，这表明大部分入射电磁波以共面极化波的形式被反射，对应的 PCR 低于 0.15，即极化转换被关闭，如图 3(c)、(d)所示，此时该结构相当于一个反射板。因此，通过控制二极管状态，该超表面实现了可开关的宽带极化转换。

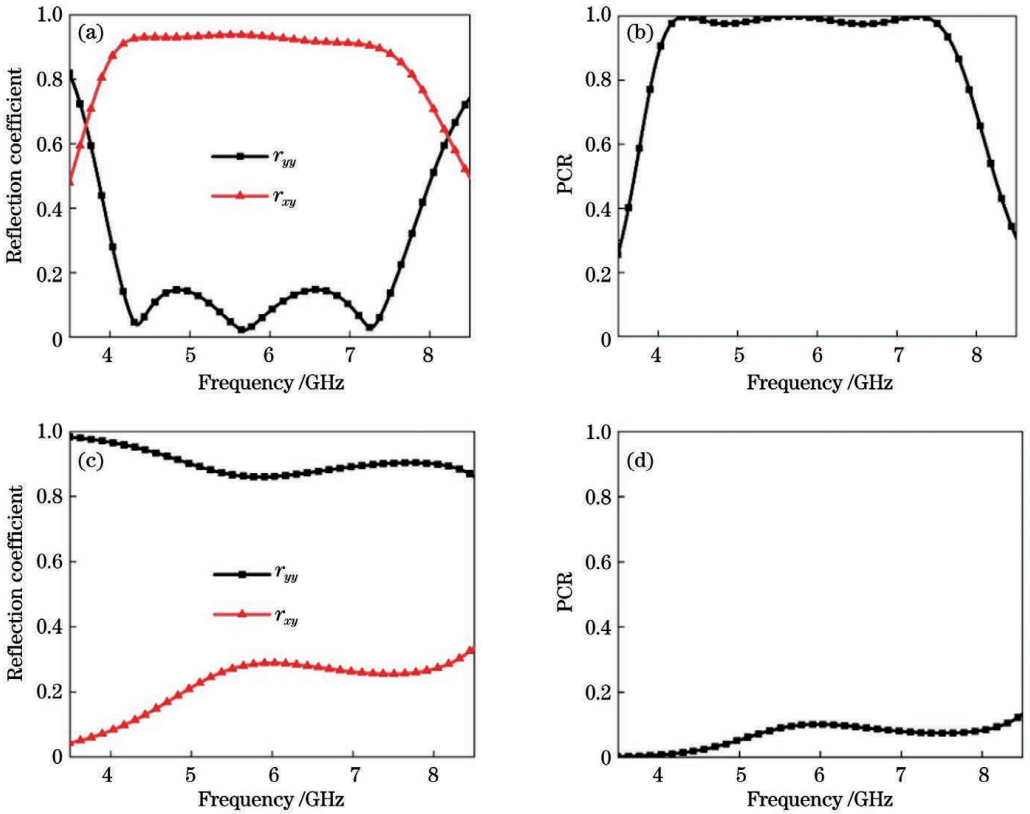

图 3　二极管处于导通或截止状态时所设计超表面的反射系数和极化转换率。(a)导通状态的反射系数；(b)导通状态的极化转换率；(c)截止状态的反射系数；(d)截止状态的极化转换率

Fig. 3　Reflection coefficients and PCR of designed metasurface when the diodes are in on-state or off-state. (a) Reflection coefficients in on-state; (b) PCR in on-state; (c) reflection coefficients in off-state; (d) PCR in off-state

所设计超表面的极化转换特性可通过其正交的本征模来解释。当电场沿着 y 轴方向极化的电磁波垂直入射到所设计的超表面时，入射电场 $\boldsymbol{E}_i$ 可以分解为沿着 u 轴方向和 v 轴方向的两个正交的本征模 E_{iu} 和 E_{iv}，如图 4(a)所示。E_{iv} 和 E_{iu} 分别平行于结构的长臂 l_1 和短臂 l_2。因此，当结构分别在 E_{iv} 和 E_{iu} 的激励下时，可以通过调整 l_1 和 l_2 的几何尺寸来确定反射波的相位。图 4(c)、(d)所示为当二极管处于导通状态时，所设计超表面分别在 E_{iv} 和 E_{iu} 的激励下，短臂长度 l_2 的变化对反射波相位的影响。从图 4(c)可以看到，在 E_{iv} 的激励下，l_2 从 2.6 mm 变化到 4.6 mm，相位 φ_v 几乎没有发生变化，这是因为短臂 l_2 垂直于 E_{iv}，l_2 的变化不会影响其相位 φ_v。而相位 φ_u 可随着 l_2 长度的变化而

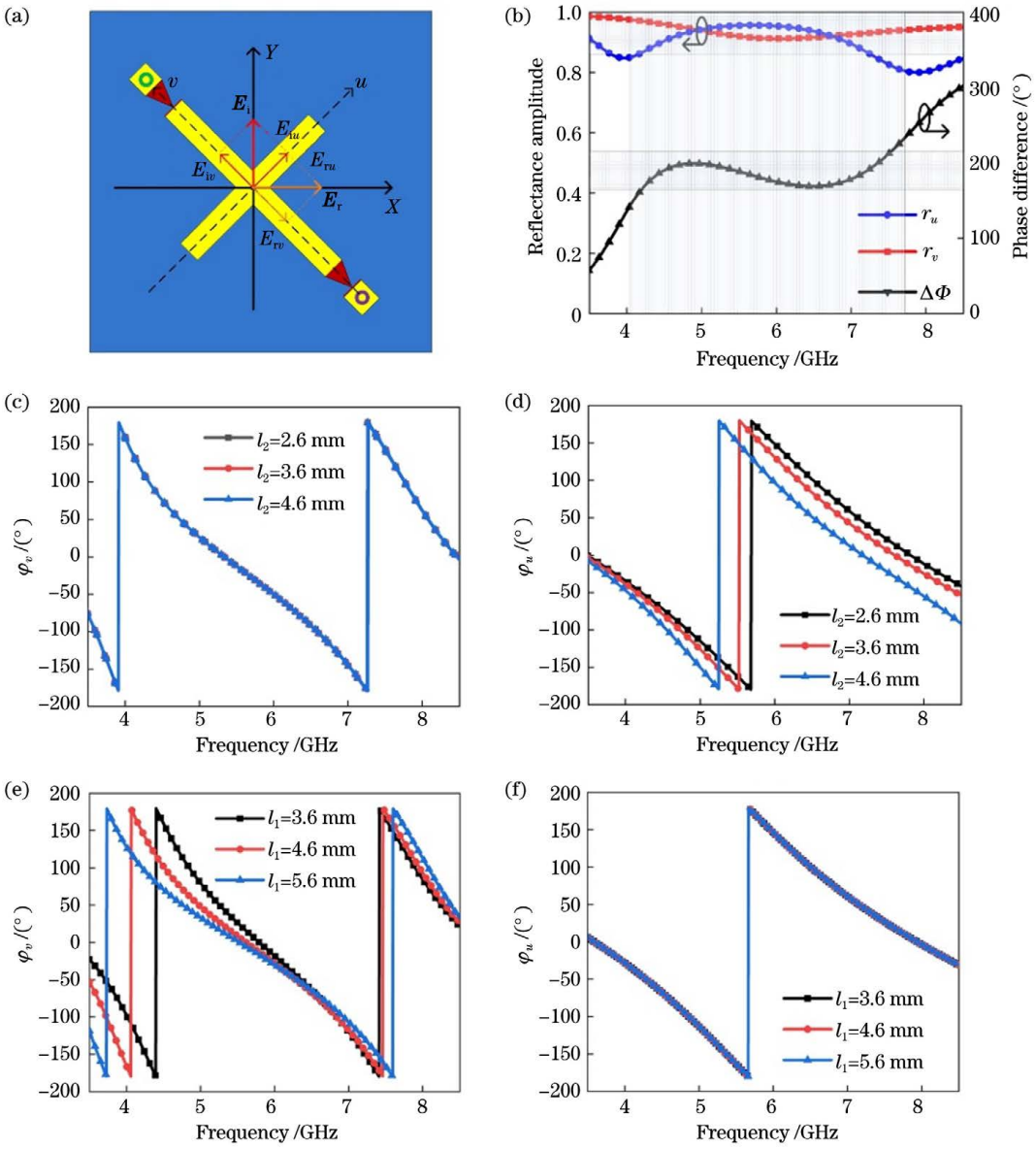

图 4　极化转换原理分析。(a)极化转换原理解析图；(b)E_{iu} 和 E_{iv} 激励下的反射系数和相位差；(c)E_{iv} 和(d)E_{iu} 激励下，l_2 变化时反射波的相位；(e)E_{iv} 和(f)E_{iu} 激励下，l_1 变化时反射波的相位

Fig. 4　Analysis of polarization conversion principle. (a) Schematic of polarization conversion; (b) reflection coefficients and phase difference under the excitation of E_{iu} and E_{iv}, respectively; reflection phases changed with the length l_2 under the excitation of (c) E_{iv} and (d) E_{iu}, respectively; reflection phases changed with the length l_1 under the excitation of (e) E_{iv} and (f) E_{iu}, respectively

调节，如图 4(d)所示，这是因为短臂 l_2 平行于 E_{iu}。同理，在 E_{iu} 的激励下，改变长臂 l_1 的长度，不会影响相位 φ_u，但会影响 φ_v，如图 4(e)、(f)所示。因此，通过选择合适的 l_1 和 l_2 可以调节 φ_v 和 φ_u 之间的相位差，从而调节反射波的极化状态。入射电场 $\boldsymbol{E}_i$ 和反射电场 $\boldsymbol{E}_r$ 可分别表示为 $\boldsymbol{E}_i=\hat{u}E_{iu}\mathrm{e}^{\mathrm{j}\varphi}+\hat{v}E_{iv}\mathrm{e}^{\mathrm{j}\varphi}$ 和 $\boldsymbol{E}_r=\hat{u}r_uE_{iu}\mathrm{e}^{\mathrm{j}(\varphi+\varphi_u)}+\hat{v}r_vE_{iv}\mathrm{e}^{\mathrm{j}(\varphi+\varphi_v)}$，其中 r_u 和 r_v 为反射波的幅度，φ_u 和 φ_v 为反射波的相位。由图 4(a)可知，当 $r_u=r_v$ 且 $\Delta\Phi=\varphi_u-\varphi_v=180°$时，电场极化方向沿 y 轴的电磁波就会被转变为沿 x 轴极化的电磁波，从而实现共面极化波向交叉极化波的转换。当 $l_1=4.6$ mm，$l_2=3.6$ mm 时，分别在 E_{iu} 和 E_{iv} 的激励下，在 4.03～7.71 GHz 工作频段，r_u 和 r_v 大致相等，$\Delta\Phi$ 也在 180°附近，如图 4(b)所示，这证实了由图 4(a)得出的结论。

为了进一步阐述所设计极化转换器的转换机制，图 5 给出了当 PIN 二极管处于导通状态时谐振频率处的表面电流分布。从图 5(a)可以看到，在谐

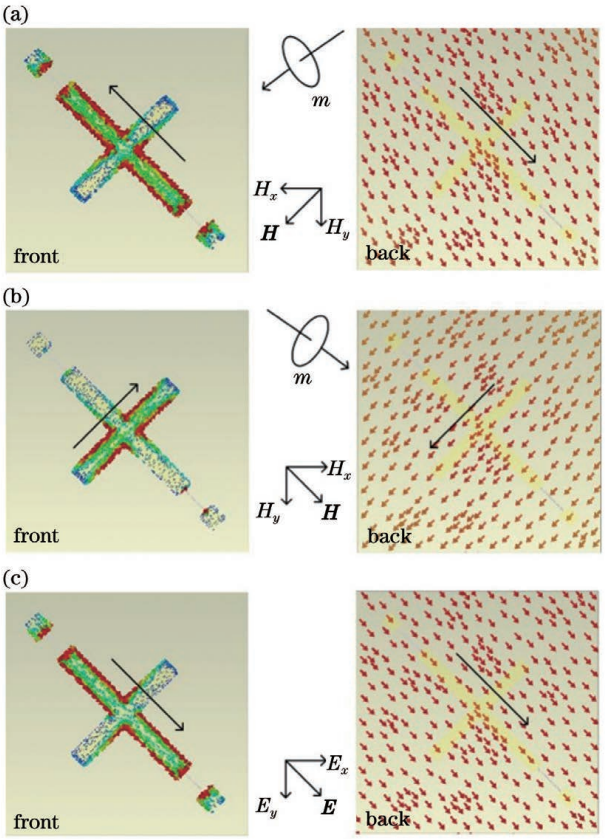

图 5 PIN 二极管处于导通状态时在不同谐振频率处的表面电流分布。(a)4.34 GHz;(b)5.67 GHz;(c)7.26 GHz

Fig. 5 Surface current distributions at different resonance frequencies when PIN diodes are in on-state. (a) 4.34 GHz; (b) 5.67 GHz; (c) 7.26 GHz

振频率点 4.34 GHz 处顶层金属谐振单元的表面电流主要分布在长臂，并与金属底板的电流形成反向平行电流，由此激发了磁偶极子 m，形成感应磁场 $\boldsymbol{H}$，其沿 y 轴方向上的分量 H_y 平行于入射电场 $\boldsymbol{E}_i$，二者交叉耦合，产生一个垂直于入射电场 $\boldsymbol{E}_i$ 的感应电场，这导致了极化转换。而感应磁场 $\boldsymbol{H}$ 沿 x 轴方向的分量 H_x 垂直于入射电场 $\boldsymbol{E}_i$，故不会产生交叉极化。同理，在 5.67 GHz 处，产生交叉极化也是因为顶层的表面电流与金属底板的电流形成磁谐振，如图 5(b)所示。而在 7.26 GHz 处，金属谐振单元的表面电流与金属底板的电流方向相同，形成电谐振，如图 5(c)所示，由此产生的感应电场 $\boldsymbol{E}$ 在 x 方向的分量 E_x 垂直于入射电场 $\boldsymbol{E}_i$，从而促进交叉极化的转换。

考虑到广角入射特性在实际工程中有着广泛的应用，考察了所设计极化转换器对倾斜入射电磁波极化转换特性的影响，结果如图 6 所示。可以看到，当入射角小于 40°时，PCR 随着入射角的增大略微降低，在工作频段内 PCR 仍大于 80%，说明所设计结构具有良好的广角入射特性。当入射角继续增大，极化转换率逐渐小于 80%，这是因为随着入射角的增大，所设计结构的电磁谐振减弱。

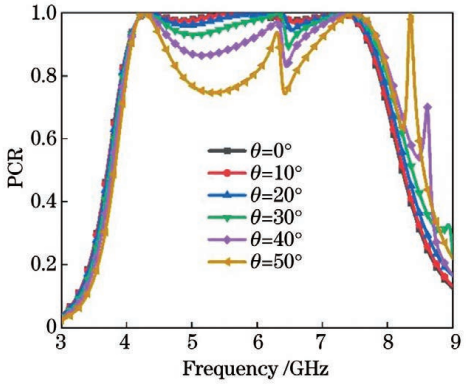

图 6 不同入射角下的 PCR

Fig. 6 PCR at different incident angles

4 样品制作及测量

为了进一步证实所设计结构的可开关极化转换特性，利用印刷电路板(printed circuit board, PCB)蚀刻技术制作了 25×25 单元结构的样品，如图 7(a)所示，单元结构的几何尺寸和仿真中的设置相同，PIN 二极管按照图 1 所示通过金属过孔和背面馈电线连接。测量环境如图 7(b)所示，采用类似 NRL 拱形测试方法[27]，利用同轴电缆和矢量网络分析仪连接发射和接收喇叭，并利用直流稳压电源给 PIN 二极管供电。将锥形泡沫吸波材料放在样品后面，以避免不必要的散射和反射干扰。

测量时，使得喇叭天线与样品之间的距离满足 NRL 标准的远场条件，为待测样品施加 2 V 的正向偏置电压，使 PIN 二极管工作在导通状态，将发射和接收喇叭水平放置，用来测量共面极化反射系数；保持发射和接收喇叭位置不变，将接收喇叭旋转 90°，用来测量交叉极化反射系数。在每一次测量前，都用与样品尺寸相同的金属板对测量设备进行校准，测量结果如图 7(c)所示。对比仿真结果可以发现，测量结果与仿真结果基本一致，但是转换带宽略微减小，测量结果有所波动，这可能是由制作以及测量误差引起的，比如旋转接收喇叭引起的误差和校准产生的误差等。在截止工作状态，给 PIN 二极管施加 20 V 反向偏置电压，用同样的方法测量共面和交叉极化反射系数，测量结果如图 7(d)所示，其 PCR 在整个工作频段都低于 0.15。综上，通过控制二极管的开关状态，该超表面完成了在极化转换和

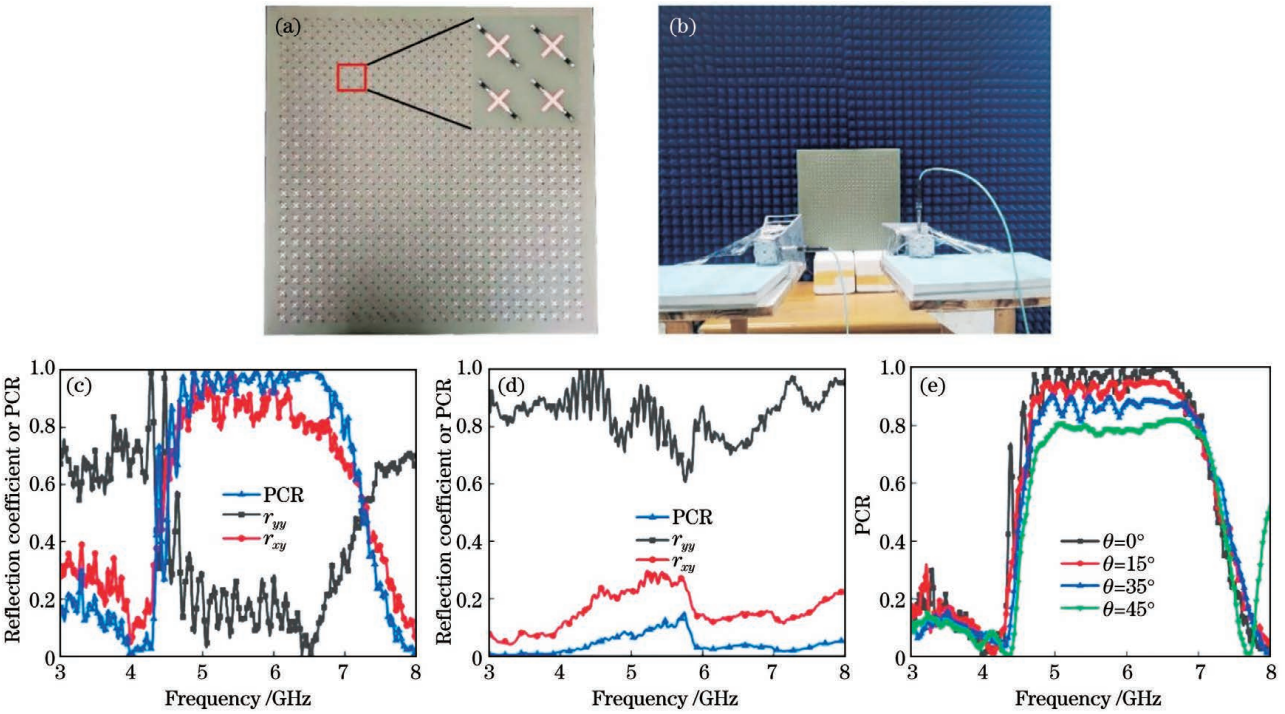

图 7 实验测量结果。(a)制作的样品;(b)测量环境;(c)二极管处于导通状态测量得到的反射系数和 PCR;(d)二极管处于截止状态测量得到的反射系数和 PCR;(e)不同入射角下的 PCR

Fig. 7 Measured results. (a) Photo of the sample; (b) measured environment; measured reflection coefficients and PCR for the diodes in (c) on-state and (d) off-state; (e) measured PCR at different incident angles

全反射功能之间的切换,调制切换的速度主要取决于二极管的开关速度,而 PIN 二极管的开关速度在纳秒量级,因此所提出的可开关超表面可以实现实时开关调控。最后,测量了斜入射角对极化转换性能的影响,结果如图 7(e)所示,可以看到,当入射角小于 45°时,PCR 基本能保持在 80%以上,表现出良好的广角入射特性。

5 结 论

基于嵌入 PIN 二极管的十字架型结构,设计了一种可开关的极化转换超表面。通过控制 PIN 二极管的工作状态,该超表面可在宽带极化转换和全反射功能间切换。仿真结果表明,当 PIN 二极管处于导通状态时,在 4.03~7.71 GHz 范围内,该超表面的极化转换率超过 90%,相对带宽为 62.7%,并且具有良好的斜入射特性。当 PIN 二极管处于截止状态时,该结构相当于一个反射板。通过理论分析和表面电流分布解释了极化转换的物理机制,且实验结果和仿真结果基本吻合。所设计的超表面有望用于电磁兼容和极化探测等领域。

参 考 文 献

[1] Sievenpiper D, Zhang L J, Broas R F J, et al. High-impedance electromagnetic surfaces with a forbidden frequency band[J]. IEEE Transactions on Microwave Theory and Techniques, 1999, 47(11): 2059-2074.

[2] Smith D R, Kroll N. Negative refractive index in left-handed materials[J]. Physical Review Letters, 2000, 85(14): 2933-2936.

[3] Pendry J B, Schurig D, Smith D R. Controlling electromagnetic fields[J]. Science, 2006, 312(5781): 1780-1782.

[4] Yan T, Ma Q, Sun S, et al. Polarization multiplexing hologram realized by anisotropic digital metasurface[J]. Advanced Theory and Simulations, 2021, 4(6): 2100046.

[5] Li L L, Cui T L, Ji W, et al. Electromagnetic reprogrammable coding-metasurface holograms[J]. Nature Communications, 2017, 8(1): 197.

[6] Gao Y F, Gu J Q, Jia R D, et al. Polarization independent achromatic meta-lens designed for the terahertz domain[J]. Frontiers in Physics, 2020, 8: 606693.

[7] Gong J, Zong R, Li H, et al. Dynamically tunable broadband terahertz metamaterial absorber based on vanadium dioxide[J]. Laser & Optoelectronics Progress, 2021, 58(3): 0316001.
龚江, 宗容, 李辉, 等. 基于二氧化钒的太赫兹超材料动态可调宽带吸收器[J]. 激光与光电子学进展,

2021, 58(3): 0316001.

[8] Cui Z J, Wang Y, Zhu D Y, et al. Perfect absorption conditions and absorption characteristics of terahertz metamaterial absorber[J]. Chinese Journal of Lasers, 2019, 46(6): 0614023.
崔子健, 王玥, 朱冬颖, 等. 太赫兹超材料吸收器的完美吸收条件与吸收特性[J]. 中国激光, 2019, 46(6): 0614023.

[9] Rao Y F, Pan L, Ouyang C M, et al. Asymmetric transmission of linearly polarized waves based on Mie resonance in all-dielectric terahertz metamaterials[J]. Optics Express, 2020, 28(20): 29855-29864.

[10] Tao X, Qi L M, Yang J, et al. Experimental verification of a broadband asymmetric transmission metamaterial in the terahertz region[J]. RSC Advances, 2020, 10(11): 6179-6184.

[11] Grady N K, Heyes J E, Chowdhury D R, et al. Terahertz metamaterials for linear polarization conversion and anomalous refraction[J]. Science, 2013, 340(6138): 1304-1307.

[12] Gao X, Han X, Cao W P, et al. Ultrawideband and high-efficiency linear polarization converter based on double V-shaped metasurface[J]. IEEE Transactions on Antennas and Propagation, 2015, 63(8): 3522-3530.

[13] Tian Y S, Guo X H, Dai L L, et al. Broadband tunable terahertz polarizers based on Dirac semimetal[J]. Chinese Journal of Lasers, 2019, 46(6): 0614033.
田元仕, 郭晓涵, 戴林林, 等. 基于狄拉克半金属宽带的可调谐太赫兹偏振器[J]. 中国激光, 2019, 46(6): 0614033.

[14] Li J X, Feng J L, Li B, et al. Dual-band transmissive cross-polarization converter with extremely high polarization conversion ratio using transmitarray[J]. Materials, 2019, 12(11): 1827.

[15] Lu T G, Qiu P Z, Lian J Q, et al. Ultrathin and broadband highly efficient terahertz reflective polarization converter based on four L-shaped metamaterials[J]. Optical Materials, 2019, 95: 109230.

[16] Nguyen T Q H, Nguyen T K T, Nguyen T Q M, et al. Simple design of a wideband and wide-angle reflective linear polarization converter based on crescent-shaped metamaterial for Ku-band applications[J]. Optics Communications, 2021, 486: 126773.

[17] Yang Z H, Jiang M Z, Liu Y C, et al. Tunable bandwidth terahertz polarization converter based on vanadium dioxide hybrid metasurface[J]. Chinese Journal of Lasers, 2021, 48(17): 1714001.
杨朝晖, 江明珠, 刘永琛, 等. 基于二氧化钒复合超表面的太赫兹带宽可调极化转换器[J]. 中国激光, 2021, 48(17): 1714001.

[18] Ma X L, Huang C, Pu M B, et al. Multi-band circular polarizer using planar spiral metamaterial structure[J]. Optics Express, 2012, 20(14): 16050-16058.

[19] Zang X F, Liu S J, Gong H H, et al. Dual-band superposition induced broadband terahertz linear-to-circular polarization converter[J]. Journal of the Optical Society of America B, 2018, 35(4): 950-957.

[20] Ghosh S K, Das S, Bhattacharyya S. Transmittive-type triple-band linear to circular polarization conversion in THz region using graphene-based metasurface[J]. Optics Communications, 2021, 480: 126480.

[21] Chang C C, Zhao Z, Li D, et al. Broadband linear-to-circular polarization conversion enabled by birefringent off-resonance reflective metasurfaces[J]. Physical Review Letters, 2019, 123(23): 237401.

[22] Wang S Y, Liu W, Geyi W. A circular polarization converter based on in-linked loop antenna frequency selective surface[J]. Applied Physics B, 2018, 124(6): 1-8.

[23] Wang M J, Zhai Z Z. Wide-angle circular polarization converter based on a metasurface of Z-shaped unit cells[J]. Frontiers in Physics, 2020, 8: 527394.

[24] Nilotpal, Nama L, Bhattacharyya S, et al. A metasurface-based broadband quasi nondispersive cross polarization converter for far infrared region[J]. International Journal of RF and Microwave Computer-Aided Engineering, 2019, 29(10): 21889.

[25] Zhou X T, Jin R C, Wang J, et al. All-metal metasurface polarization converter in visible region with an in-band function[J]. Applied Physics Express, 2019, 12(9): 092010.

[26] BA591 Band-switching diode[EB/OL]. [2021-04-21]. https://www.nxp.com/docs/en/data-sheet/BA591.pdf.

[27] Hofmann W, Bornkessel C, Schwind A, et al. Challenges of RF absorber characterization: comparison between RCS- and NRL-arch-methods[C]// 2019 International Symposium on Electromagnetic Compatibility-EMC Europe, 2-6 September, 2019, Barcelona, Spain. New York: IEEE Press, 2019: 370-375.

Switchable Broadband Polarization Conversion Metasurface Based on PIN Diodes

Li Damin[1], Wang Jiayun[1], Su Xiaoqiang[2], Dong Lijuan[2*], Chen Xinwei[1], Zhang Wenmei[1], Yang Rongcao[1**]

[1] *School of Physics & Electronic Engineering, Shanxi University, Taiyuan, Shanxi* 030006, *China*;

[2] *Shanxi Province Key Laboratory of Microstructure Electromagnetic Functional Materials, Shanxi Datong University, Datong, Shanxi* 037009, *China*

Abstract

Objective Since the artificial metasurface was proposed, it has attracted extensive attention owing to its unique physical properties and wide applications in many fields, such as holographic imaging, microstrip antenna, absorber, and polarization converter. The polarization converter is an important research topic in the application of metasurfaces. Currently, single-band, multiband, and broadband polarization conversion metasurfaces have been developed, and their operating frequency bands cover the microwave, terahertz, infrared, and visible bands. However, most of the traditional polarization converters lack switchable performance. Although the frequency or amplitude values of some metasurfaces are tunable, the methods are complex. Herein, a switchable and high-efficiency broadband polarization conversion metasurface is designed with PIN diodes. By controlling the state of the diodes, the switchable polarization conversion is realized, and the measured and simulation results agree excellently, which verifies the switchable polarization conversion of the metasurface. Compared with the traditional polarization conversion metasurface, the proposed structure may be applied in practical engineering to meet special requirements. The design enriches the research of metasurfaces and provides a strategy for switchable polarization converters.

Methods In the simulation, electromagnetic (EM) simulation software, CST, based on the finite integration technique (FIT), was adopted to simulate the proposed polarization conversion metasurface. Periodic boundary conditions (unit cell) were set along the x and y directions, the EM wave propagated along the negative z-axis, and the electric and magnetic fields were polarized along the y and x axes, respectively. The polarization conversion rate (PCR) is defined as $R_{\mathrm{PCR}} = |r_{xy}|^2/(|r_{xy}|^2 + |r_{yy}|^2)$, where r_{yy} and r_{xy} are the co-polarization and cross-polarization reflection coefficients, respectively. In the experimental measurement, a 25×25 unit structure sample was built by adopting printed circuit board (PCB) etching technology; the overall size of the sample is 400 mm × 400 mm. The PIN diodes were embedded in the structures, and a DC stabilized power supply provided the bias voltage for the diodes. The wedge foam materials were placed behind the sample to eliminate the interference from scattering and unnecessary reflection. The sample was measured in free space using the approximate NRL arch method, the transmitting and receiving angles were connected to the vector network analyzer through a low-loss coaxial cable, respectively, and the distance between the angles and the sample meets the far-field conditions of the NRL standard. First, the forward bias voltage of 2 V was applied on the sample, and the two angles were horizontally placed to measure the co-polarization waves. Next, the positions of the transmitting horns were maintained, and rotated the receiving angle was rotated by 90° to receive the cross-polarization reflection waves. Before each measurement, the different pieces of measuring equipment were calibrated using a metal plate of the same size as the sample.

Results and Discussions Here, a switchable polarization conversion metasurface was designed and fabricated. PIN diodes were embedded in the appropriate position of the metasurface to control the operating states. Bottom feed lines were designed to provide bias voltage for the diodes. The metasurface schematic is shown in Fig. 1. When the diodes are in the on state, ranging from 4.03–7.71 GHz, the co-polarization reflection coefficient is less than 0.2, the cross-polarization reflection coefficient exceeds 0.9, and the corresponding PCR exceeds 0.9, indicating that broadband and high-efficiency polarization conversion is achieved. However, when the diodes are in the off state, the co-polarization reflection coefficient exceeds 0.8, the cross-polarization reflection coefficient is less than 0.3, and the corresponding PCR is less than 0.15. In this case, the metasurface works as a reflector. Therefore, the proposed polarization conversion metasurface has a good switching polarization conversion performance (Fig. 3).

Furthermore, the principle of polarization conversion was explained by analyzing the orthogonal eigenmodes (Fig. 4) and the surface current distributions at the resonant frequency (Fig. 5). Additionally, the wide-angle incidence characteristics of the metasurface were investigated; when the incident angle increases to 40°, the PCR still exceeds 80% in the working frequency band (Fig. 6). Finally, a sample of the polarization conversion metasurface was built, indicating that the measured and simulation results agree excellently (Fig. 7).

Conclusions By embedding the PIN diodes in the metasurface and delicately designing the feed circuit, a cross-shaped switchable polarization conversion metasurface is proposed. When the diodes are in the on state, the metasurface works in the polarization conversion mode, the PCR exceeds 90% in the range of 4.03–7.71 GHz, and the corresponding relative bandwidth is 62.7%. However, when the diodes are in the off state, the polarization conversion is turned off, and the metasurface works as a reflector. The mechanism of the polarization conversion metasurface is explained by theoretical analysis and surface current distributions. The designed metasurface has good wide-angle incident characteristics, and the metasurface has good polarization performance within the incident angle of less than 45°. Furthermore, the measured and simulation results agree excellently, which confirms the feasibility of this work. The proposed metasurface is expected to be used in EM compatibility and polarization detection.

Key words materials; metasurface; switchable polarization conversion; PIN diode; broadband